A&A 643, A60 (2020)
https://doi.org/10.1051/0004-6361/201936598

Astronomy & Astrophysics

Distribution of methanol and cyclopropenylidene around starless cores⋆,⋆⋆

S. Spezzano[1], P. Caselli[1], J. E. Pineda[1], L. Bizzocchi[1], D. Prudenzano[1], and Z. Nagy[1,2]

[1] Max Planck Institute for Extraterrestrial Physics, Giessenbachstrasse 1, 85748 Garching, Germany
e-mail: spezzano@mpe.mpg.de
[2] Konkoly Observatory, Research Centre for Astronomy and Earth Sciences, 1121 Budapest, Konkoly Thegeút 15–17, Hungary

Received 29 August 2019 / Accepted 1 September 2020

ABSTRACT

Context. The spatial distribution of molecules around starless cores is a powerful tool for studying the physics and chemistry governing the earliest stages of star formation.
Aims. Our aim is to study the chemical differentiation in starless cores to determine the influence of large-scale effects on the spatial distribution of molecules within the cores. Furthermore, we want to put observational constraints on the mechanisms responsible in starless cores for the desorption of methanol from the surface of dust grains where it is efficiently produced.
Methods. We mapped methanol, CH_3OH, and cyclopropenylidene, c-C_3H_2, with the IRAM 30 m telescope in the 3 mm band towards six starless cores embedded in different environments, and in different evolutionary stages. Furthermore, we searched for correlations among physical properties of the cores and the methanol distribution.
Results. From our maps we can infer that the chemical segregation between CH_3OH and c-C_3H_2 is driven by uneven illumination from the interstellar radiation field (ISRF). The side of the core that is more illuminated has more C atoms in the gas-phase and the formation of carbon-chain molecules like c-C_3H_2 is enhanced. Instead, on the side that is less exposed to the ISRF the C atoms are mostly locked in carbon monoxide, CO, the precursor of methanol.
Conclusions. We conclude that large-scale effects have a direct impact on the chemical segregation that we can observe at core scale. However, the non-thermal mechanisms responsible for the desorption of methanol in starless cores do not show any dependency on the H_2 column density at the methanol peak.

Key words. astrochemistry – line: identification – ISM: molecules

1. Introduction

Stars form in dense cloud cores that can be studied through the emission of cold dust and molecules. Molecules, in particular, carry very precious information, and studying the chemical structure of dense cores is important to reveal the process of star formation and the chemical evolution from clouds to stars and planets. Starless cores are the earliest stages in the formation of low-mass stars. The more dynamically evolved cores among starless cores are the pre-stellar cores, gravitationally unstable cores on the verge of collapse to form a protostar. The key evolutionary factors that define a pre-stellar core are extensively described in Crapsi et al. (2005), among which are the high abundance of N_2H^+ and N_2D^+, high deuterium fractionation, high CO freeze-out towards the centre of the core, and central density higher than 5×10^5 cm^{-3} (see also Keto & Caselli 2008). Small-scale effects influence the chemical differentiation in starless cores. The enhanced deuteration observed in the inner regions of starless cores, for example, is caused by the local physical properties of the centre of starless cores: low temperatures (5–10 K) and high densities (10^5–10^6 cm^{-3}) (Caselli et al. 2003).

The chemical segregation of methanol, CH_3OH, and cyclopropenylidene, c-C_3H_2, towards the pre-stellar core L1544 is discussed in Spezzano et al. (2016). The different spatial distribution of c-C_3H_2 and CH_3OH can be related to the uneven illumination around the core, a large-scale effect. While c-C_3H_2 traces the southern part of the core, where a sharp drop in the H_2 column density is present, CH_3OH traces the northern part of the core, characterised by a shallower tail of H_2 column density. This differentiation can be related to the fraction of carbon locked in carbon monoxide, CO. In the south of L1544, photochemistry maintains more C atoms in the gas phase, and consequently increases the production of carbon-chain molecules. In the north of L1544, C is mainly locked in CO, the precursor for the formation of methanol on dust grain. The emission maps of 22 different molecules were observed towards the same core, and it was shown that all oxygen-bearing molecules have their emission peak towards the north of the core, and show a similar distribution to methanol (Spezzano et al. 2017). In order to test the universality of the above-mentioned results on L1544, we decided to study the chemical differentiation in six starless cores in different evolutionary stages, and embedded in different environments.

Furthermore, studying the distribution of methanol around starless cores is essential to understand the physical and chemical processes, still poorly understood, that are responsible for its desorption from the icy mantles of dust grains. Methanol is the simplest complex organic molecule (COM, defined as

⋆ The reduced datacubes are only available at the CDS via anonymous ftp to cdsarc.u-strasbg.fr (130.79.128.5) or via http://cdsarc.u-strasbg.fr/viz-bin/cat/J/A+A/643/A60

⋆⋆ Based on observations carried out with the IRAM 30 m Telescope. IRAM is supported by INSU/CNRS (France), MPG (Germany), and IGN (Spain).

carbon-containing molecules with more than five atoms, Herbst & van Dishoeck 2009) observed in the ISM, and the one whose formation reactions are better studied and constrained. Gas-phase reactions fail to reproduce the high abundances of methanol observed towards hot cores and corinos (Garrod & Herbst 2006; Geppert et al. 2006). On the other hand, laboratory experiments show that methanol can be efficiently formed through the hydrogenation of carbon monoxide frozen on the icy mantle of dust grains (Watanabe & Kouchi 2002). Hot core and hot corinos are high temperature regions ($T \geq 100$ K) surrounding high- and low-mass protostars, respectively. The observation of large fractional abundances of methanol relative to molecular hydrogen towards hot cores and hot corinos can be explained with methanol evaporating from the grains when the medium is warmed up by the protostar. Explaining the large fraction of methanol observed around starless cores is more problematic because the mechanism of thermal desorption from dust grains must be ruled out due to the absence of a nearby heating source. Recent laboratory works show that photodesorption of methanol from dust grains cannot be the mechanism responsible for the gas-phase methanol observed around starless cores (Bertin et al. 2016; Cruz-Diaz et al. 2016) as the methanol will mostly desorb as fragments and not as a whole. Alternative routes for an efficient desorption of methanol from the icy mantles at low temperatures are the reactive or chemical desorption (Vasyunin et al. 2017), low-velocity shocks caused by accretion of material onto the core (Punanova et al. 2018), and sputtering due to cosmic rays (Dartois et al. 2019). Because methanol is the starting point of chemical complexity in the ISM, understanding the processes responsible for its release in the gas phase is of pivotal importance in order to constrain chemical models and reproduce the chemical complexity that we observe in space.

This paper is structured as follows: the source sample and the observations are described in Sect. 2, the chemical segregation observed between c-C_3H_2 and CH_3OH is described in Sect. 3, the abundance profiles of methanol and cyclopropenylidene are presented in Sect. 4, a discussion about methanol in starless cores is presented in Sect. 5. In Sect. 6 we summarise our results and present our conclusions.

2. Observations

2.1. Source sample

Our source sample, listed in Table 1, covers a wide range of evolutionary stages and environmental conditions. Among the six cores mapped, four are considered pre-stellar following the definition given in Crapsi et al. (2005), namely L429, L694-2, OphD, and HMM-1. B68 is an isolated starless core, called a Bok globule, located in the south with respect to the Ophiucus molecular cloud. Depletion of N_2H^+ and $C^{18}O$ has been observed towards this source (Bergin et al. 2002). B68 was included in our study because it is relatively isolated, and hence supposed to be exposed to uniform external illumination. Therefore, we expect the segregation among c-C_3H_2 and CH_3OH to be minimised. L429, in the Aquila Rift molecular cloud, is the core with the highest H_2 column density in our sample and is characterised by a very high deuterium fraction in N_2H^+ (Crapsi et al. 2005). L694-2 is a pre-stellar core with structural and chemical properties similar to L1544 (Lee et al. 2004; Crapsi et al. 2005). L1521E is a starless core in Taurus, the same molecular cloud where L1544 is located, but it is not as evolved (Tafalla & Santiago 2004; Nagy et al. 2019). OphD and HMM-1 are two pre-stellar cores in Ophiucus. B68, L694-2, and L1521E are embedded in a homogeneous interstellar radiation field (ISRF), and hence the illumination on the core only depends on the density structure around it. B68 is a particular case because it is an isolated core and as a consequence even illumination can be assumed. L429, OphD, and HMM-1 are instead embedded in active environments (Redaelli et al. 2018; de Geus 1992; Preibisch & Mamajek 2008), and the presence of nearby stars, as well as the density structure around the core, has an influence on the illumination on it. Our aim is to check whether large-scale effects, like illumination, can indeed be responsible for the chemical differentiation that we observe at core scales.

2.2. IRAM 30 m

The maps presented in this paper, shown in Figs. 1 and A.1, were observed using the Eight MIxer Receiver (EMIR) E090 instrument of the IRAM 30 m telescope (Pico Veleta) in on-the-fly mode with position switching. The off positions are 3′ from the dust peak. The molecular transitions, observed in a single set-up, are reported in Table 2. The Fourier transform spectrometer (FTS) was used as the backend with a spectral channel resolution of 50 kHz, about 0.15 km s^{-1} in the 3 mm frequency range. The observations were carried out in June and August 2016. The antenna moved along an orthogonal pattern of linear paths separated by 8″ intervals, corresponding to roughly one-third of the beam full width at half maximum (FWHM). The mapping was carried out in good weather conditions ($\tau \sim 0.03$) and a typical system temperature of $T_{sys} \sim 90$–100 K. A single set-up was used, and the typical noise level per spectral channel resolution is between 15 and 30 mK km s^{-1}. The data processing was done using the GILDAS software (Pety 2005). A typical second-order polynomial baseline was used for all the sources. All the emission maps presented in this paper are gridded to a pixel size of 4″ with the CLASS software in the GILDAS package, which corresponds to 1/5-1/7 of the actual beam size, depending on the frequency. The velocity ranges used to calculate the integrated intensities are reported in Table 1.

2.3. Herschel/SPIRE

The large-scale maps presented in this paper were dowloaded from the ESA *Herschel* Science Archive[1]. We computed the total column density of H_2, $N(H_2)$, and the dust temperature, T_{dust}, using the three Spectral and Photometric Imaging Receiver (SPIRE) bands at 250, 350, and 500 μm, for which the pipeline reduction includes zero-level corrections based on comparison with the *Planck* satellite data (Griffin et al. 2010). The maps of $N(H_2)$ and T_{dust} are shown in Figs. 2 and B.1. A modified blackbody function with the dust emissivity spectral index $\beta = 2.0$ was fitted to each pixel, after smoothing the 250 and 350 μm maps to the resolution of the 500 μm image (~40″) and resampling all images to the same grid. For the dust emissivity coefficient we adopted the value from Hildebrand (1983), $\kappa_{250\,\mu m} = 0.1$ cm^2 g^{-1}, and used the power law approximation

$$\kappa_\nu = \kappa_{\nu_0} \left(\frac{\nu}{\nu_0} \right)^\beta ,$$

where κ_{ν_0} is the opacity at a reference frequency 250 μm. A dust-to-gas mass ratio of 0.01 is assumed. The $N(H_2)$ peak value for each source is listed in Table 1. All *Herschel* maps presented in this paper have a size of 9×9 arcmin^2. The T_{dust} maps are in the Appendix.

[1] http://archives.esac.esa.int/hsa/whsa/

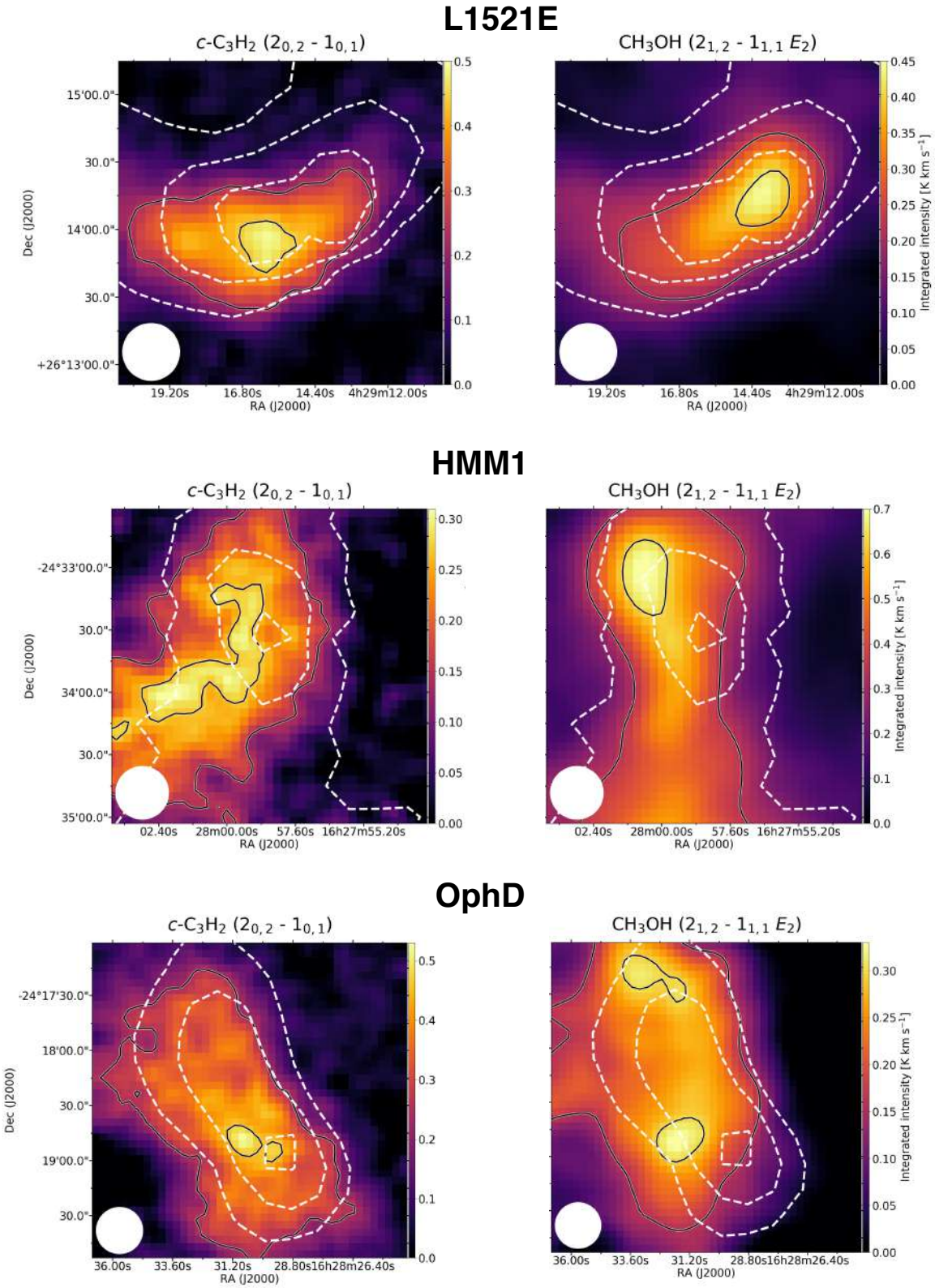

Fig. 1. Integrated emission maps of (*left*) c-C_3H_2 and (*right*) CH_3OH towards the sources in our sample. The solid line contours indicate 90 and 50% of the integrated intensity peak for all molecules with the exception of the $2_{0,2}-1_{0,1}$ (E_1) CH_3OH transition in L429, where the contours indicate 90 and 65% of the integrated intensity peak. The dashed line contours represent the A_V values computed from the *Herschel*/SPIRE maps (5, 10, and 15 mag for B68; 20, 40, and 70 mag for L429; 10, 15, and 20 mag for L1521E; 20, 40, and 80 mag for L694-2; 20, 40, and 60 mag for HMM-1; 20, 30, and 40 mag for OphD). The white circle in the bottom left corner of each panel shows the 40″ beam of the SPIRE data.

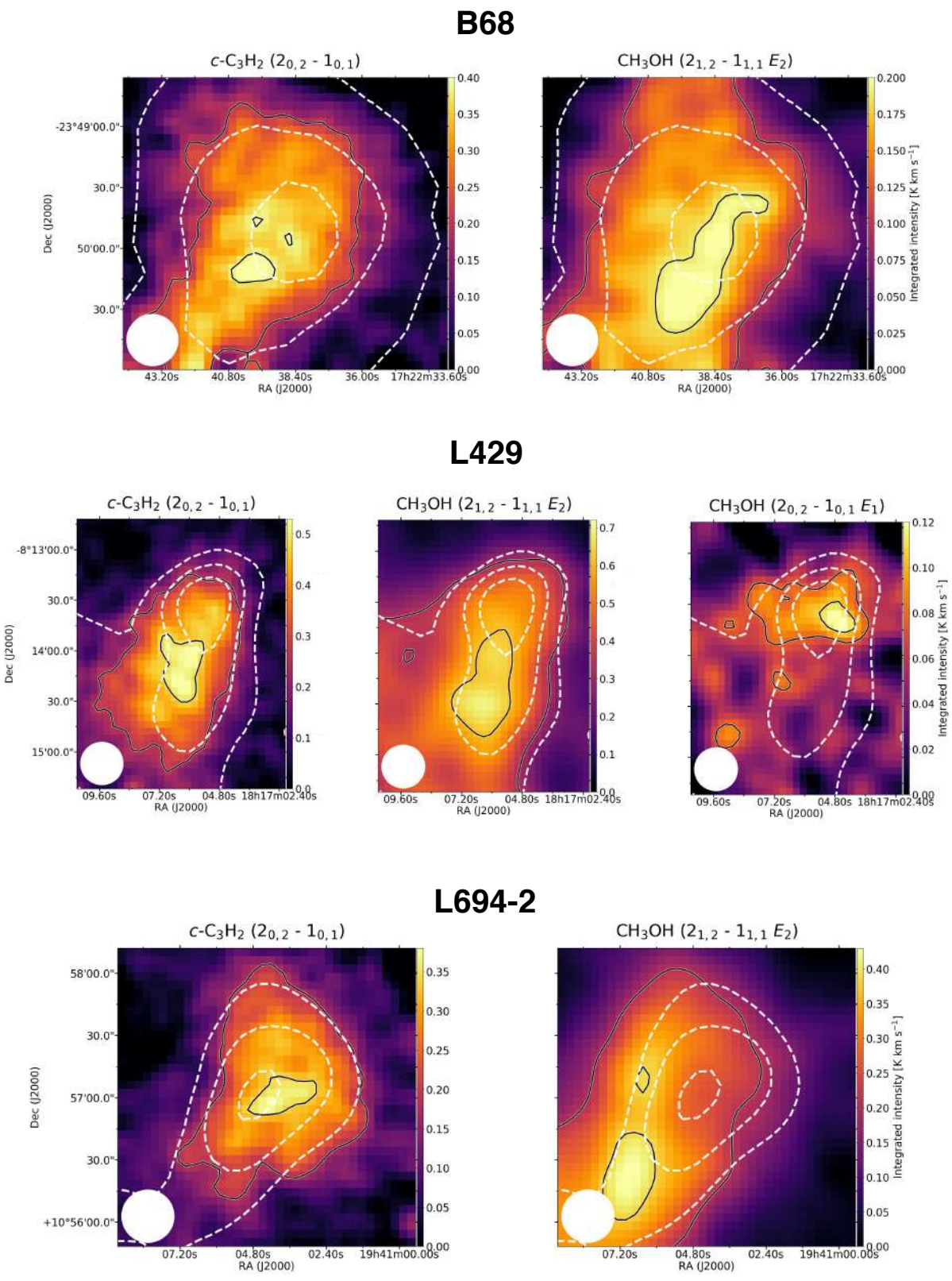

Fig. 1. continued.

3. Results

We present here the maps of methanol ($J_{K_a,K_c} = 2_{1,2}–1_{1,1}$, E_2) and cyclopropenylidene ($J_{K_a,K_c} = 2_{0,2}–1_{0,1}$) towards two starless and four pre-stellar cores with the IRAM 30 m telescope (Fig. 1). A segregation between the two molecules is present towards all cores in our sample except for B68. Given the broadband capabilities of the receivers at the IRAM 30 m telescope, we were able to map several molecules simultaneously. In Spezzano et al. (2017) it was shown that towards the prototypical pre-stellar core L1544

Table 1. Sources.

	Right ascension (J2000)	Declination (J2000)	V_{LSR} (km s^{-1})	Distance [a] (pc)	H_2 column density [b] (10^{22} cm^{-2})	Velocity range [c] (km s^{-1})	Map size 30 m ($'' \times ''$)
L1521E (s) [d]	04:29:15.7	+26:14:05.0	6.7	140	2.5	6.2–7.3	70 × 70
HMM-1 (p)	16:27:58.3	−24:33:42.0	4.3	140	6	3.7–4.6	75 × 85
OphD (p)	16:28:30.4	−24:18:29	3.5	140	4	3.2–4.0	85 × 85
B68 (s)	17:22:38.9	−23:49:46	3.4	150	1.4	2.9–3.7	80 × 80
L429 (p)	18:17:6.40	−08:14:00	6.7	436	10	6.2–7.4	75 × 85
L694-2 (p)	19:41:04.5	+10:57:02	9.6	230	8	9.2–10	70 × 70

Notes. [a]B68: Alves & Franco (2007), L429, OphD and HMM-1: Ortiz-León et al. (2018), L694-2: Kawamura et al. (2001), L1521E: Galli et al. (2018). [b]Value computed from *Herschel*/SPIRE observations towards the dust peak. [c]Velocity ranges where the integrated emission has been computed. [d]Starless (s) or pre-stellar (p), following the definition given in Crapsi et al. (2005).

Table 2. Spectroscopic parameters of the observed lines.

Molecule	Transition	Rest frequency [a] (MHz)	E_{up} (K)	A ($\times 10^{-5}$ s^{-1})	n^{*} [b] cm^{-3}
c-C_3H_2	$J_{K_a,K_c} = 2_{0,2}$–$1_{0,1}$	82 093.544(1)	6.43	1.89	5×10^5
CH_3OH	$J_{K_a,K_c} = 2_{1,2}$–$1_{1,1}$ (E_2)	96 739.358(2)	12.53 [c]	0.26	3×10^4
CH_3OH	$J_{K_a,K_c} = 2_{0,2}$–$1_{0,1}$ (E_1)	96 744.545(2)	20.08 [c]	0.34	3×10^4
CCS	$N_J = 6_7$–5_6	81 505.17(2)	15.39	2.43	–
C_4H	$N = 9$-8, $J = 19/2$-17/2, $F = 9$-9 & 9-8	85 364.004(3) & 85 364.015(3)	20.55	0.26	–

Notes. [a]Frequencies and uncertainties from the CDMS (Müller et al. 2005). [b]n* is the critical density, calculated at 10 K. [c]Energy relative to the ground $0_{0,0}$, A rotational state.

all carbon-chain molecules trace the same part of the core (the c-C_3H_2 peak), while oxygen-bearing molecules peak towards a different part of the pre-stellar core (the methanol peak). Sulphur does not seem to play a key role in the spatial distribution, with OCS and SO peaking towards the methanol peak and CCS and H_2CS peaking at the c-C_3H_2 peak. Based on previous studies of L1544 (Spezzano et al. 2016, 2017), we decided to use, when available, the maps of CCS and C_4H to check if the emission structure of cyclopropenylidene, of which we have mapped only one transition, is indeed representative of the distribution of carbon chain molecules. For the methanol line, we use instead the $2_{0,2}$–$1_{0,1}$ (E_1) transition, when available, because it is slightly higher in energy than the $2_{1,2}$–$1_{1,1}$ (E_2) transition, and hence less optically thick. These additional maps are reported in Fig. A.1. Given the frequency resolution of our dataset, 50 kHz, we cannot exclude the effect of self-absorption on the maps, nor did we observe enough lines of methanol and cyclopropenylidene to be able to precisely derive the T_{ex}, and hence the optical depth of the mapped transitions. Assuming an excitation temperature of 5 K, we calculated the optical depth of the mapped transitions towards the dust peak in each source (see Table 3). The line opacity τ is defined as

$$\tau = \ln\left(\frac{J(T_{ex}) - J(T_{bg})}{J(T_{ex}) - J(T_{bg}) - T_{mb}}\right), \quad (1)$$

where $J(T) = \frac{h\nu}{k}(e^{\frac{h\nu}{kT}} - 1)^{-1}$ is the equivalent Rayleigh-Jeans temperature in Kelvin, k is the Boltzmann constant, ν is the frequency of the line, h is the Planck constant, and T_{ex}, T_{bg}, T_{mb} arethe excitation, the background (2.7 K), and the main beam temperatures respectively, in K. We assume an excitation temperature of 5 K for all levels (Caselli et al. 2002). This temperature assumption gives a τ of 0.87 for the lines of

Table 3. Optical depth of the mapped lines at 5 K.

	c-C_3H_2 ($2_{0,2}$–$1_{0,1}$)	CH_3OH ($2_{1,2}$–$1_{1,1}$, E_2)
L1521E	0.87(5)	0.62(4)
HMM-1	0.34(3)	0.87(8)
OphD	0.62(4)	0.38(3)
B68	0.7(1)	0.26(4)
L429	0.57(4)	0.87(6)
L694-2	0.57(5)	0.34(3)

Notes. Numbers in parentheses are one standard deviation in units of the least significant digits.

c-C_3H_2 towards L1521E, and of methanol towards HMM-1 and L429, showing moderately high optical depth. The properties of all observed transitions are given in Table 2. The critical densities of the two methanol transitions are calculated based on the Einstein coefficients and collisional rates in the LAMDA catalogue (Schöier et al. 2005); instead, for the cyclopropenylidene transitions we use the collisional rates reported in Ben Khalifa et al. (2019). The critical densities are not reported for C_4H and CCS because the collisional coefficients are not present in the LAMDA catalogue. Furthermore, in order to check whether the illumination around the core has an influence on the distribution that we observe, we plot the contours of both molecules on the H_2 column density and T_{dust} maps that we computed from the *Herschel*/SPIRE observations (Fig. 2). To facilitate the comparison among the different cores, the contours from the SPIRE maps are reported in visual extinction, calculated as A_V [mag] = $N(H_2)$[cm^{-2}]/9.4×10^{20} [cm^{-2} mag^{-1}]

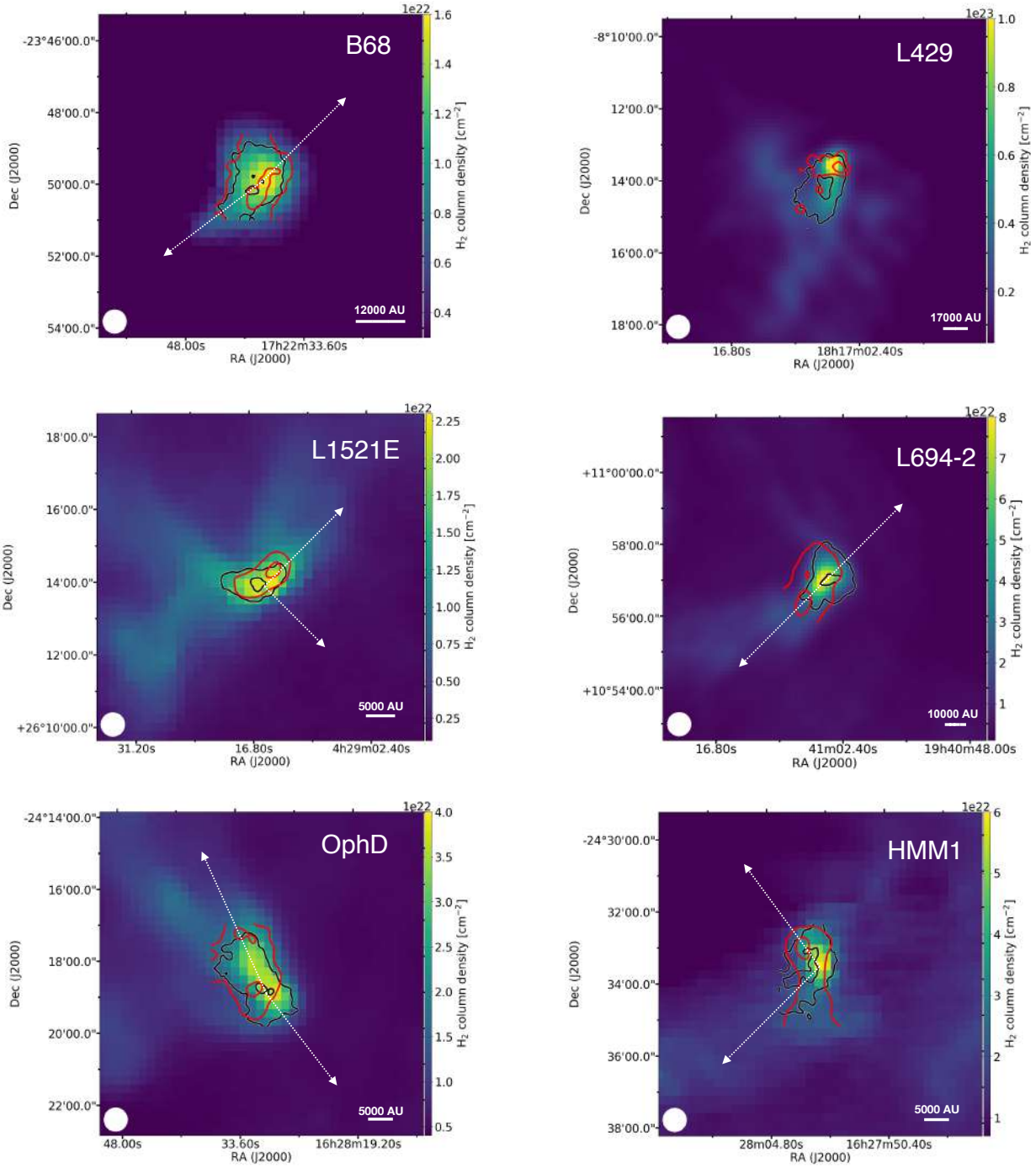

Fig. 2. 9 × 9 arcmin^2 H_2 column density maps computed from *Herschel*/SPIRE data. The red and black contours represent 90 and 50% of the integrated intensity peak of CH_3OH and c-C_3H_2, respectively. The white circle in the bottom left of each panel shows the 40″ beam of the SPIRE data. The dotted white arrows (not present for L429) indicate the directions in which the abundances profiles discussed in Sect. 4 were extracted.

(Bohlin et al. 1978). The spectra of methanol and cyclopropenylidene extracted at the dust peak of each of the sources in our sample are shown in Fig. 3. All lines are fitted with a Gaussian profile, and the corresponding parameters are given in Table 4. Given the low spectral resolution of the observations (~0.15 km s^{-1}), we cannot infer detailed information about the kinematics of the sources in our sample. Nevertheless, we can confirm the same results reported in Spezzano et al. (2016) for methanol and cyclopropenylidene in L1544: despite the different spatial distribution, both molecules trace similar kinematic patterns in all sources in our sample, and have similar line widths.

3.1. L1521E

The maps of CH_3OH and c-C_3H_2 observed towards L1521E are shown in Fig. 1. Even if it is not as pronounced as in other cores in our sample, a chemical segregation between the two molecules is present in L1521E, with the methanol peaking in the northwest and the cyclopropenylidene towards the centre or southern part of the core. The spatial distribution of c-C_3H_2 is confirmed to follow those of the maps of C_4H and CCS, and the distribution of the E_2 methanol line is consistent with the map of the E_1 methanol line shown in the appendix (Fig. A.1). We can hence

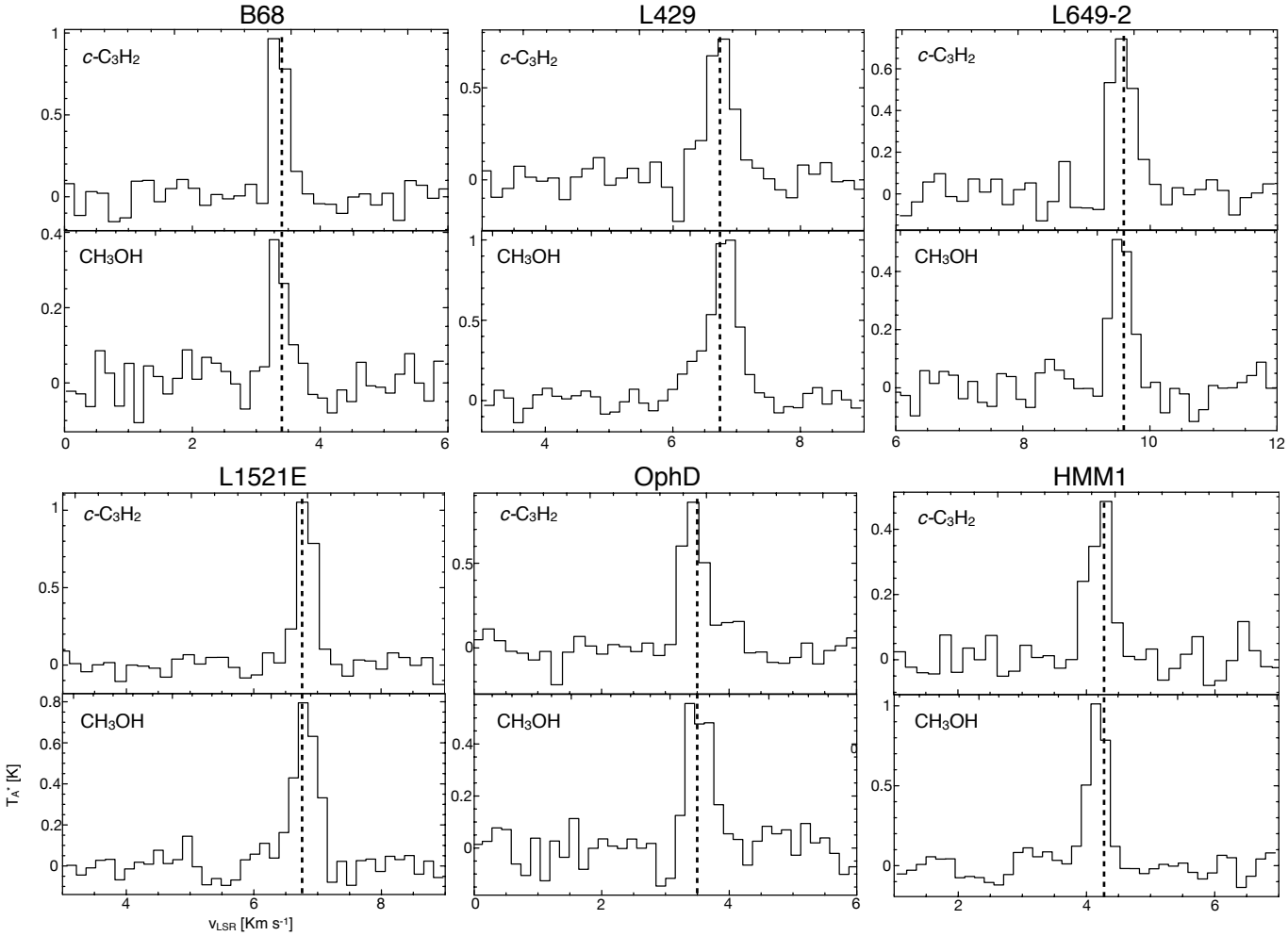

Fig. 3. Spectra of the $J_{K_a,K_c} = 2_{0,2}-1_{0,1}$ transition of cyclopropenylidene and of the $J_{K_a,K_c} = 2_{1,2}-1_{1,1}$ (E_2) transition of methanol towards the dust peak of the sources in our sample. The dotted vertical line shows the systemic velocity of the sources listed in Table 1.

assume that the moderately high optical depth of the c-C_3H_2 transition reported in Table 3 is not affecting the morphology of the distribution. As can be seen in the large-scale maps shown in Fig. 2, the southern part of the core is the most exposed to the ISRF.

3.2. HMM-1

Also in HMM-1, methanol and cyclopropenylidene trace different parts of the core, with methanol tracing the eastern part, and the cyclopropenylidene surrounding it, as shown in Fig. 1. The emission map of CCS in the appendix (Fig. A.1) confirm that carbon-chain molecules trace the north-west part of HMM-1. The optical depth of the $2_{1,2}-1_{1,1}$ (E_2) methanol line is moderately high (see Table 3). In order to check whether the optical depth has an impact on the structure of its emission, we present the map of the $2_{0,2}-1_{0,1}$ (E_1) transition of methanol in Fig. A.1, which shows the same spatial distribution of the $2_{1,2}-1_{1,1}$ (E_2) line. However, the large-scale maps in Fig. 2, seem to contradict what has been observed towards L1544. The density in HMM-1 has a sharper drop towards the eastern side where methanol peaks. This can however be explained by the presence of the B-type stars ρ Oph and HD 147889 towards the west with respect to HMM-1 (de Geus 1992; Preibisch & Mamajek 2008). The increase in the kinetic temperature towards HD 147889 in the ρ Ophiucus molecular cloud was measured by observing hyperfine anomalies in the OH 18 cm line (Ebisawa et al. 2015). Furthermore, the effect of HD 147889 on the region was studied with maps of CI, CII, and CO, showing an arrangement that is in contrast to the prediction of plane-parallel PDR models and can be explained as significant density gradients, as well as different chemical evolution (Kamegai et al. 2003). When considering that HMM-1 is embedded in a non-homogeneous ISRF because of a strong illumination from the west due to the stars, for HMM-1 the differentiation between CH_3OH and c-C_3H_2 also follows the trend seen in L1544 and in the other cores described in this paper. The asymmetry of the methanol distribution in HMM-1 is discussed in Harju et al. (2020).

3.3. OphD

The chemical segregation between c-C_3H_2 and CH_3OH in OphD is clearly visible in Fig. 1. The methanol emission is elongated and has two emission peaks, while that of cyclopropenylidene is more concentrated towards the dust peak of the core. Figure A.1 shows the emission maps of C_4H and CCS, which confirm that carbon-chain molecules in OphD trace the south-western part of the core. The emission of the E_1 methanol line could not be mapped because it is too weak. In the large-scale map in Fig. 2 we show that the methanol emission is farther away from the

Table 4. Observed line parameters of CH_3OH and c-C_3H_2.

Molecule	Transition ($J'_{K'_aK'_c}$-$J''_{K''_aK''_c}$)	Area (K km s^{-1})	V_{LSR} (km s^{-1})	Δv (km s^{-1})
		L1521E		
c-C_3H_2	$2_{0,2}$–$1_{0,1}$	0.40(2)	6.82(1)	0.32(2)
CH_3OH	$2_{1,2}$–$1_{1,1}$	0.35(2)	6.81(1)	0.41(3)
		HMM-1		
c-C_3H_2	$2_{0,2}$–$1_{0,1}$	0.23(2)	4.21(2)	0.45(4)
CH_3OH	$2_{1,2}$–$1_{1,1}$	0.39(2)	4.17(1)	0.35(2)
		OphD		
c-C_3H_2	$2_{0,2}$–$1_{0,1}$	0.38(3)	3.43(2)	0.41(4)
CH_3OH	$2_{1,2}$–$1_{1,1}$	0.28(2)	3.53(2)	0.45(4)
		B68		
c-C_3H_2	$2_{0,2}$–$1_{0,1}$	0.32(2)	3.35(1)	0.22(7)
CH_3OH	$2_{1,2}$–$1_{1,1}$	0.12(2)	3.34(2)	0.27(6)
		L429		
c-C_3H_2	$2_{0,2}$–$1_{0,1}$	0.40(3)	6.73(2)	0.47(5)
CH_3OH	$2_{1,2}$–$1_{1,1}$	0.55(3)	6.80(1)	0.52(3)
		L694-2		
c-C_3H_2	$2_{0,2}$–$1_{0,1}$	0.35(3)	9.56(2)	0.42(3)
CH_3OH	$2_{1,2}$–$1_{1,1}$	0.23(2)	9.54(2)	0.38(3)

Notes. Numbers in parentheses are one standard deviation in units of the least significant digit.

edge of the core, hence the more illuminated side where the carbon chain molecules peak. As already discussed for HMM-1, the presence of the B-type stars ρ Oph and HD 147889 also has an effect on OphD (Fig. 2) with the difference that in OphD the sharper drop in density, hence the more illuminated side, faces the west where the B-type stars are also located, and both contribute to an active hydrocarbon chemistry.

3.4. B68

Figure 1 shows the emission maps of c-C_3H_2 and CH_3OH, observed towards the inner 80 arcsec × 80 arcsec of B68 with the IRAM 30 m telescope. The distribution of the two molecules is similar and without a preferential position around the starless core. The spatial distribution of c-C_3H_2 is confirmed by the map of C_4H shown in Fig. A.1. The emission of the E_1 methanol line could not be mapped because it is too weak. The large-scale map in Fig. 2 confirms that B68 is indeed an isolated globule and not part of a more complex density structure, while the other cores in our sample are. As a consequence, we can infer that a homogeneous ISRF surrounds B68.

3.5. L429

No chemical segregation can be inferred from the observed emission maps of c-C_3H_2 and CH_3OH $2_{1,2}$–$1_{1,1}$ (E_2) towards L429 as both molecules seem to trace the same region within the core, as shown in Fig. 1.

The central H_2 column density of L429 is seven times higher than B68, the least dense core in our sample, and about a factor of 2 higher than all the other cores, with the exception of L694-2 and L1544. Given the high density of the core, and the high brightness temperature of the lines mapped, the absence of chemical differentiation could be an effect due to the optical depth of the lines, or self-absorption. As was done for HMM-1, also in this case we checked the map of the $2_{0,2}$–$1_{0,1}$ (E_1) transition of methanol, shown in Fig. 1. The $2_{0,2}$–$1_{0,1}$ (E_1) transition of methanol shows a different spatial distribution with respect to the $2_{1,2}$–$1_{1,1}$ (E_2) transition, hinting at the fact that the spatial distribution of the $2_{1,2}$–$1_{1,1}$ (E_2) transition might be affected by optical depth and/or self-absorption. We investigated this issue further and used the CASSIS software[2] (Vastel et al. 2015) to model the observed spectra of methanol towards the dust peak in L429. It is not possible to reproduce the relative intensity among the three methanol lines ($2_{0,2}$–$1_{0,1}$ E_1, $2_{1,2}$–$1_{1,1}$ E_2, and $2_{0,2}$–$1_{0,1}$ A^+) at 96.7 GHz without using a non-LTE approach. When modelling the spectra with the LTE assumption with an excitation temperature of either 5 or 4 K, we overestimate the intensity of the $2_{0,2}$–$1_{0,1}$ (E_1) line, the highest in energy among the three. This is not the case towards all the other sources in our sample, where the intensity ratio among the three methanol lines can always be reproduced with LTE, assuming an excitation temperature of 5 K. When using the non-LTE radiative transfer code RADEX (van der Tak et al. 2007) within the software CASSIS, we can reproduce well the spectrum assuming a T_{kin} of 10 K, a H_2 volume density of 6×10^5 cm^{-3} (Crapsi et al. 2005), and a $N(CH_3OH)$ of $\sim 5 \times 10^{13}$ cm^{-2}. The resulting T_{ex} is 9.5 K for the $2_{1,2}$–$1_{1,1}$ (E_2) transition, and 8 K for the $2_{0,2}$–$1_{0,1}$ (E_1) transition. Furthermore, the resulting optical depth for the $2_{1,2}$–$1_{1,1}$ (E_2) line is only 0.3, suggesting that the line is not necessarily optically thick, but rather that the system is out of LTE.

The presence of multiple components along the line of sight might also play a role towards L429. Redaelli et al. (2018) show that the line width of N_2H^+ in L429 is broader than in L183 and L694-2. This could be due to environmental effects (e.g. higher levels of turbulence), but also to the presence of multiple components along the line of sight. We note that the double peak seen in N_2H^+ (1–0) has been interpreted as due to self-absorption in a contracting cloud, based on detailed non-LTE modelling (Keto & Caselli 2008, 2010; Keto et al. 2015). Nevertheless, Crapsi et al. (2005) showed that the broad lines of N_2H^+ towards the dust peak of L429 have a hint of a double peak while not showing the classical blue-asymmetry attributed to infall, thus suggesting the presence of two velocity components. Considering that the H_2 column density of L429 is exceptionally high within our sample, as well as the results of Crapsi et al. (2005) and Redaelli et al. (2018), it is plausible to assume the presence of multiple components along the line of sight.

In Fig. A.1 we show the emission maps of CCS and C_4H, which both trace the same region traced by c-C_3H_2. Figure 2 shows the large-scale maps of $N(H_2)$ and T_{dust} computed from SPIRE with the contours of c-C_3H_2 and CH_3OH observed with the 30 m telescope. Because of the above-mentioned optical depth effects, we chose to plot the contours of the $2_{0,2}$–$1_{0,1}$ (E_1) transition of methanol instead of the $2_{1,2}$–$1_{1,1}$ (E_2). Contrary to what happens in L1544, in L429 methanol traces the part of the core that is facing the steepest decrease in H_2 column density, the north side, and hence the most illuminated part according to the SPIRE maps. Cyclopropenylidene instead traces the southern part of L429. The discrepancy among the two sources might be due to the different environment surrounding the two cores. The Aquila Rift is an active star-forming region that does not allow us to assume a homogeneous ISRF around L429. The closest star to L429, IRAS 18158-0813, is less than 0.5° towards the east (Kwok et al. 1997), and the brightest nearby source is a C-star, IRAS 18156-0653, located at 1.5° towards the north (Kim et al. 2013). On the contrary, L1544 does not have any protostars or young

[2] http://cassis.irap.omp.eu

stars nearby, and the asymmetry of the c-C_3H_2–CH_3OH distribution correlates well with the density structure that surrounds the core (Spezzano et al. 2016).

3.6. L694-2

The chemical differentiation between methanol and cyclopropenylidene in L694-2 is clearly shown in Fig. 1. While methanol traces the south-eastern side of the core, cyclopropenylidene traces the central and western parts of the core. The spatial distribution of c-C_3H_2 is confirmed by the map of CCS shown in Fig. A.1. The emission of the E_1 methanol line could not be mapped because it is too weak. When looking at the large-scale maps presented in Fig. 2, it is clear that the segregation in L694-2 is similar to that observed in L1544 (Spezzano et al. 2016), with the methanol tracing a side of the core that is more shielded from the ISRF with respect to the side traced by cyclopropenylidene.

4. Abundances profiles

In order to study quantitatively the dependence of the segregation between c-C_3H_2 and CH_3OH on the large-scale structure around the core, we computed the column density maps for both molecules in each core in our sample, and in L1544. Subsequently, we extracted the $N(CH_3OH)/N(c\text{-}C_3H_2)$ ratios in two directions, starting from the core's dust peak. These directions were defined following the cometary shape of starless and pre-stellar cores, already recognised in Crapsi et al. (2005), and are indicated in Fig. 2 by dotted white arrows. They either point towards the "head" or the "tail" of the comet-like structure of the core. The head is intended as the sharp drop in H_2 column density, while the tail is a shallower drop. In the case of B68 there is not a proper tail because the core is isolated, and the profile defined as tail in Fig. 4 is the one pointing towards the south-east in Fig. 2. Given the small extent of the methanol $2_{0,2}-1_{0,1}$ (E_1) line map, it was not possible to extract the profiles for L429. For L1544, the data used in this section were extracted in the profiles shown in Fig. 1 of Spezzano et al. (2016), with the head being the profile pointing towards the south-west, and the tail being the profile pointing towards the north-east.

The column densities were calculated following the formula reported in Mangum, & Shirley (2015) for the non-optically thin approximation. The total column density is defined as

$$N_{\rm tot} = \frac{8\pi\nu^3 Q_{\rm rot}(T_{\rm ex})W}{c^3 A_{\rm ul} g_{\rm u}} \frac{e^{\frac{E_{\rm u}}{kT}}}{J(T_{\rm ex}) - J(T_{\rm bg})} \frac{\tau}{1-e^{-\tau}}, \quad (2)$$

where τ is the optical depth of the line defined in Eq. (1), c is the speed of light, $A_{\rm ul}$ is the Einstein coefficient of the transition, $g_{\rm u}$ is the degeneracy of the upper state, $E_{\rm u}$ is the energy of the upper state, and $Q_{\rm rot}$ is the partition function of the molecule at the given temperature $T_{\rm ex}$. To calculate $N_{\rm tot}$ as we did for τ, we assumed a $T_{\rm ex}$ of 5 K for both molecules. The effect of using different excitation temperatures for methanol and cyclopropenylidene on the derived column density ratios was tested and found to be not significant (when decreasing the temperature by 1 K, the effect on the ratio was of the order of 20%). The error introduced by using a constant excitation temperature to calculate the column density map in a pre-stellar core was found to be negligible in a previous study of L1544 (see the Appendix of Redaelli et al. 2019). By using these expressions, we assumed that the source fills the beam, and the emission obeys LTE. The values of methanol and cyclopropenylidene column densities, as well as the values of A_V, are averaged within the SPIRE data beam (40″) and are extracted with a step of 1/3 of a beam. Unfortunately, we cannot use non-LTE radiative transfer codes to derive the column densities of CH_3OH and c-C_3H_2 towards the different profiles in our sources because the physical models available are spherically symmetric (usually a Bonnor-Ebert sphere), and hence cannot reproduce the asymmetry in our maps. In order to assess the impact that non-LTE effects might have on our results, we calculated the deviation of the LTE assumption in a range of volume densities between 1×10^4 and 1×10^6 cm^{-3}. We find that while the LTE assumption might underestimate the $N(CH_3OH)/N(c\text{-}C_3H_2)$ abundance ratio by a factor of 2–3, it does not vary strongly with volume density, and hence it does not have an effect on the trends that we discuss in this section and show in Fig. 4. More details are given in Appendix C.

Figure 4 shows the profiles of the $N(CH_3OH)/N(c\text{-}C_3H_2)$ abundance ratios as well as the visual extinction A_V towards both the tail and the head in all the cores in our sample. The errors on the A_V are comparable to the errors estimated for the H_2 column density computed from the SPIRE data, namely ~20% (see e.g. Chantzos et al. 2018). The error bars on the A_V values are not shown to avoid overcrowding the plots. In all cores where a substantial difference in the $N(CH_3OH)/N(c\text{-}C_3H_2)$ abundance ratio between the tail and the head is present (L1521E, L694-2, L1544, and OphD), a correspondent substantial difference can be seen in the A_V at larger radii. B68, being an isolated core, does not have a tail or head structure, and does not have a differentiation among the two molecules. HMM-1 shows a hint of anti-segregation, with the $N(CH_3OH)/N(c\text{-}C_3H_2)$ abundance ratio increasing towards the head rather than towards the tail. As already mentioned, this can be explained by the active environment where HMM-1 is embedded, where the presence of two B-type stars towards the west makes the illumination on that side of the core more prominent, despite its density structure, and hence does describe the segregation based solely on the head and tail structure of the core. In the case of OphD, also located in Ophiucus nearby HMM-1, the head is facing the west, and hence the illumination of the nearby stars contributes to the spatial segregation among methanol and cyclopropenylidene in the core. This effect can be seen in Fig. 5, where we plot for each source the ratio of $N(CH_3OH)/N(c\text{-}C_3H_2)$ in the two profiles (tail and head) at the largest observed offset in the 30 m data (R), against the ratio among the A_V towards the tail and the head of the core. The three cores embedded in a homogeneous ISRF (L1521E, L1544, and L694-2) show a clear increase in R with increasing A_V ratio in the tail. OphD shows the largest R in our sample even without having the highest A_V ratio in the tail, hinting at the presence of an additional factor that increases the segregation between CH_3OH and c-C_3H_2. In our opinion this effect is due to the presence of the stars nearby. B68 shows no segregation ($R=1$), and confirms the linear correlation among R and the A_V ratio shown by L1521E, L1544, and L694-2.

5. Methanol in starless cores

Non-thermal desorption mechanisms play a crucial role in the development of chemical complexity in starless cores, and starless cores set the initial conditions for the chemical complexity in the processes of star and planet formation. It is therefore critical to understand the interplay of the different chemical and physical processes at play in starless cores. Methanol has been observed in several starless cores (Soma et al. 2015;

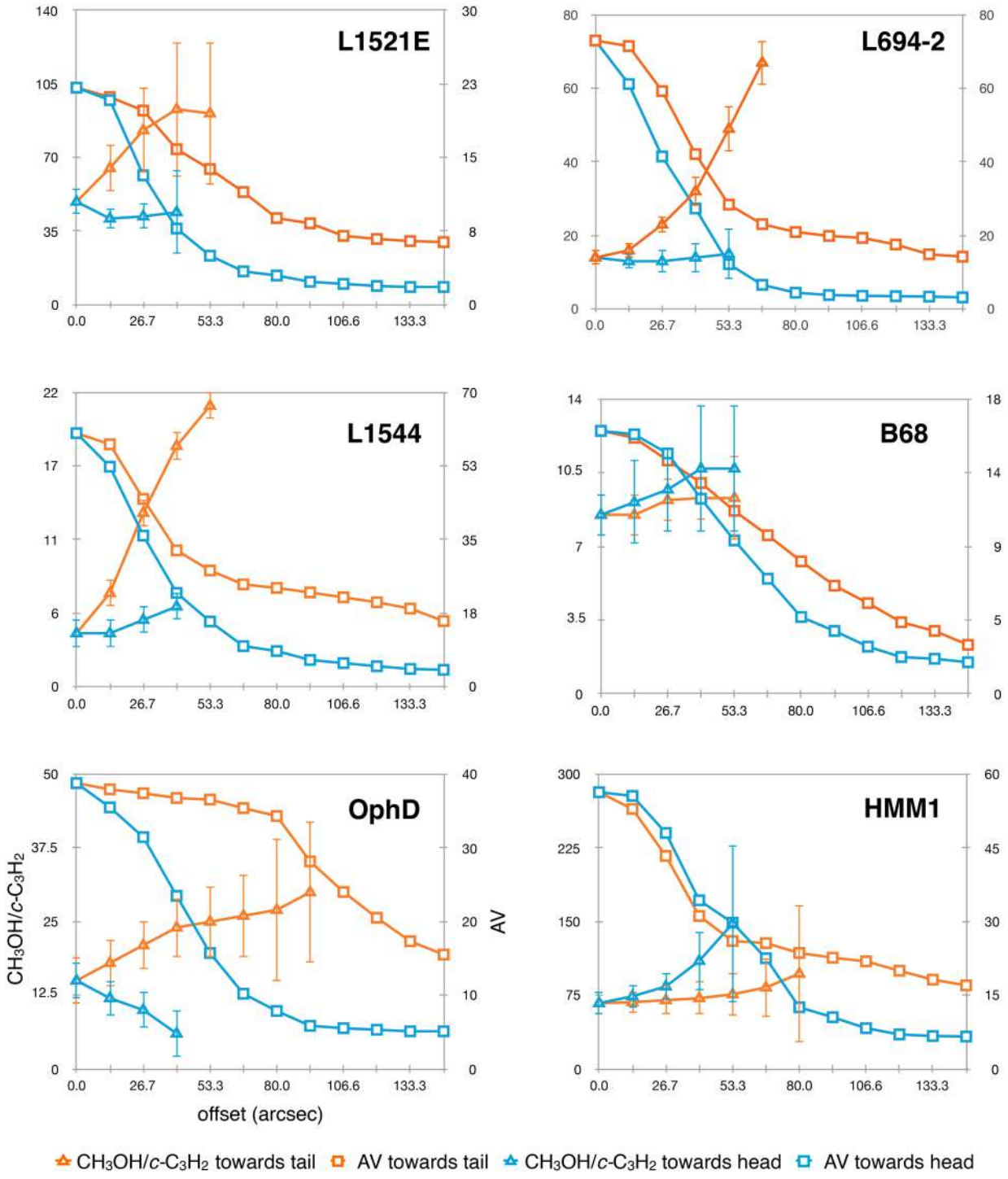

Fig. 4. $N(CH_3OH)/N(c\text{-}C_3H_2)$ abundance ratios and the visual extinction A_V extracted towards both the tail and the head in all the cores in our sample. The dotted white arrows in Fig. 2 indicate the directions in which the abundances profiles were extracted.

Vastel et al. 2014), and mapped in a few (Bizzocchi et al. 2014; Tafalla et al. 2006). With the present dataset we can correlate the distribution of methanol around six starless cores, seven if we also include L1544 in the sample, to the physical properties of the cores, with the aim of putting some observational constraints on the chemical models. In Table 5 we report the visual extinction, the T_{dust} and the $N(CH_3OH)$ values at the methanol peak, as well as the distance of the methanol peak from the *Herschel* dust peak, the central H_2 column density for each core, and the methanol abundance at the methanol peak. The A_V at the methanol peak varies from 14 in B68 to 96 in L429 (at the peak of the $2_{0,2}-1_{0,1}$ (E_1) transition); this large spread suggests that the processes responsible for the desorption of methanol in the gas phase are not too sensitive to H_2 column density variations within the column density ranges in Table 5. This result is consistent with the expectation that CH_3OH requires high enough A_V for efficient surface production and release in the gas phase. Vasyunin et al. (2017) presented the results of a gas-grain astrochemical model which includes the reactive desorption to model the abundance of complex organic molecules towards pre-stellar

Table 5. Methanol peak properties.

	A_V [(a)] (mag)	T_{dust} [(b)] (K)	Central $N(H_2)$ [(c)] (10^{22} cm^{-2})	$N(CH_3OH)$ [(d)] $\times 10^{13}$ cm^{-2}	Distance from dust peak (au)	$N(CH_3OH)/N(H_2)$ [(e)] $\times 10^{-9}$
L1521E	23(3)	12(2)	2.5(4)	12.0(7)	2000	6(1)
HMM-1	39(6)	12(2)	6.0(9)	18(2)	6000	5(1)
OphD	26(4)	12(4)	4.0(6)	8.0(6)	7000	3.3(8)
B68	14(2)	13(2)	1.4(2)	5(1)	6000	4(1)
L429	96(14)	10(1)	10(1)	2.8(7)	7000	0.3(1)
L694-2	23(3)	11(2)	8(1)	11(1)	13 000	5(1)
L1544	36(5)	11(2)	6.0(9)	12(1)	4000	3.5(9)

Notes. Numbers in parentheses are one standard deviation in units of the least significant digits. [(a)]A_V at methanol peak. [(b)]T_{dust} at methanol peak. [(c)]Value computed from *Herschel*/SPIRE observations towards the dust peak. [(d)]$N(CH_3OH)$ at methanol peak. [(e)]The methanol abundance at the methanol peak is averaged within the *Herschel* beam (40″).

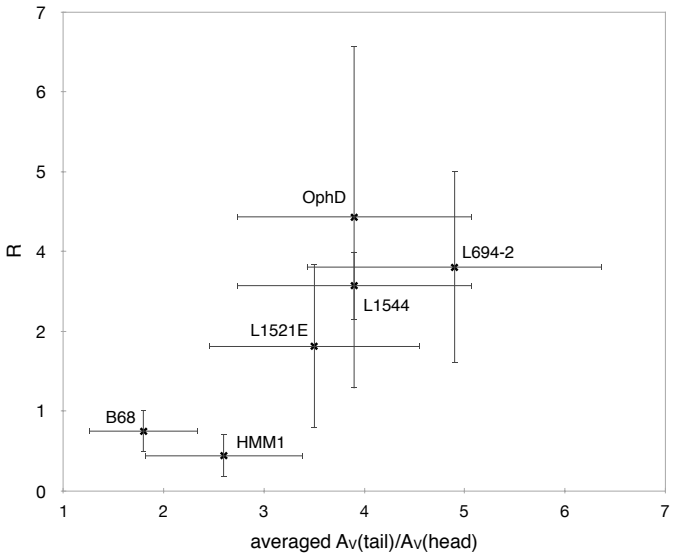

Fig. 5. Ratio of the abundance ratios $N(CH_3OH)/N(c\text{-}C_3H_2)$ in the head and tail profiles at the largest observed offset (R) plotted against the ratio of the averaged A_V towards the head and tail of each core.

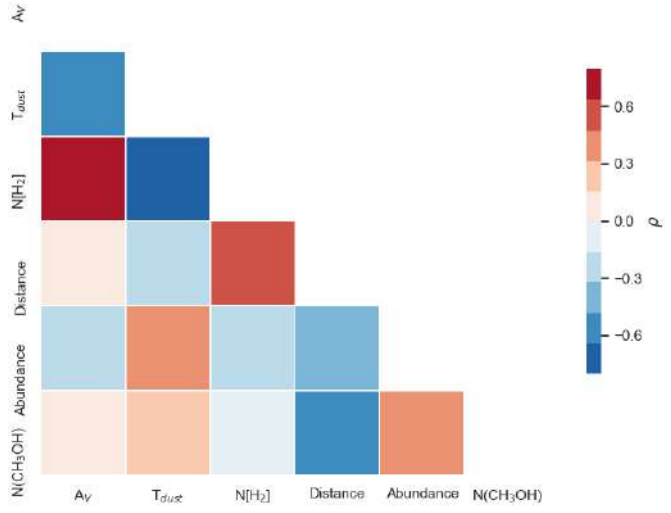

Fig. 6. Diagonal correlation matrix showing the Spearman correlation coefficients ρ among the methanol peak properties in Table 5.

cores. The results presented in Vasyunin et al. (2017) show that by using the physical structure for the pre-stellar core L1544 (Keto & Caselli 2010) complex organic molecules peak at radial distances between 0.01 and 0.03 pc, which in L1544 correspond to a visual extinction of 7 magnitudes. We note that the extinction given in Fig. 2 of Vasyunin et al. (2017) is the model extinction seen by the core, and does not consider the cloud where the core is embedded. With the *Herschel* observations, instead, we see the total extinction. The model extinction from Vasyunin et al. (2017) needs to be multiplied by a factor of two to be compared with the value observed with *Herschel*, and reported in Table 5 of this paper.

To check if there is any interdependence among the parameters listed in Table 5, we calculated the Spearman correlation coefficient ρ among them. The results are shown in a diagonal correlation matrix in Fig. 6. The only strong correlations found are between the A_V at the methanol peak and the central H_2 column density, and the T_{dust} at the methanol peak and the central H_2 column density, both $\rho \simeq 0.7$. Given the lack of correlation between the abundance of methanol and the central H_2 column density of the core, the correlations between the A_V and T_{dust} at the methanol peak and the central H_2 column density are very likely to be dependent on the evolutionary state of the core rather than on the desorption mechanism of methanol. A moderate correlation ($\rho \simeq 0.5$) is found between the central density and the distance of the methanol peak from the dust peak, which suggests that the location of the methanol peak, and hence the formation of methanol in starless and pre-stellar cores, depends on the physical structure and evolution of the core. Interestingly, the methanol abundance with respect to molecular hydrogen does not show any correlation with the other parameters listed in Table 5. Additional observations are needed to put more constraints on the interdependence of the physical and chemical evolution in the earliest stages of star formation. In particular large maps of different isotopologues of carbon monoxide will be useful to understand the link between the formation–desorption of methanol and the CO freeze-out.

6. Conclusions

We compared the spatial distribution of methanol and cyclopropenylidene in two starless and four pre-stellar cores at different evolutionary stages and embedded in different environments, and conclude that large-scale effects have a direct impact on the chemical segregation that we observe at core-scale. Methanol and cyclopropenylidene trace different regions

and give us complementary views of dense cloud cores, thus enriching our understanding of the complex interplay between physics and chemistry in the early stages of star formation. The conclusions that we draw by observing crucial molecular tracers prove once again the importance of astrochemistry in the field of star formation. With the present study we showed that there is a correlation among the abundance ratio of methanol and cyclopropenylidene within the core and the large-scale density structure around the core. More observational studies are needed in order to better constrain the physical structure of these core, and in particular how they merge into the parent cloud. This is needed for the radiative transfer modelling of the molecular emission maps.

We also used our dataset to put observational constraints on the non-thermal desorption of methanol in starless cores. We find that the methanol peaks in a wide range of H_2 column densities in the different cores in our sample, suggesting that while the formation of methanol requires a high visual extinction ($A_V > 7$ mag) for both its production on the grains and its release in the gas-phase, the H_2 column density is not a crucial parameter in the non-thermal desorption of methanol in starless cores. Our results suggest instead that the central density of the core might have an influence on the distance between the dust peak and the methanol peak. Given the importance of methanol in the development of complex organic chemistry in star-forming regions, more observational studies, both with single-dish telescopes and interferometers, should be performed in order to put more constraints on the chemical models, and finally shine some light on the release in the gas-phase of methanol in starless cores.

Acknowledgements. The authors wish to thank the anonymous referee and the editor for insightful comments, and are grateful for the support by the Max Planck Society.

References

Alves, F. O., & Franco, G. A. P. 2007, A&A, 470, 597
Ben Khalifa, M., Sahnoun, E., Wiesenfeld, L., et al. 2019, Phys. Chem. Chem. Phys. , 21, 1443
Bergin, E. A., Alves, J., Huard, T., & Lada, C. J. 2002, ApJ, 570, L101
Bertin, M., Romanzin, C., Doronin, M., et al. 2016, ApJ, 817, L12
Bizzocchi, L., Caselli, P., Spezzano, S., & Leonardo, E. 2014, A&A, 569, A27
Bohlin, R. C., Savage, B. D., & Drake, J. F. 1978, ApJ, 224, 132
Caselli, P., Benson, P. J., Myers, P. C., et al. 2002, ApJ, 572, 238
Caselli, P., van der Tak, F. F. S., Ceccarelli, C., & Bacmann, A. 2003, A&A, 403, L37
Chantzos, J., Spezzano, S., Caselli, P., et al. 2018, ApJ, 863, 126
Crapsi, A., Caselli, P., Walmsley, C. M., et al. 2005, ApJ, 619, 379
Cruz-Diaz, G. A., Martín-Doménech, R., Muñoz Caro, G. M., & Chen, Y.-J. 2016, A&A, 592, A68
Dartois, E., Chabot, M., Id Barkach, T., et al. 2019, A&A, 627, A55
de Geus, E. J. 1992, A&A, 262, 258
Ebisawa, Y., Inokuma, H., Sakai, N., et al. 2015, ApJ, 815, 13
Galli, P. A. B., Loinard, L., Ortiz-Léon, G. N., et al. 2018, ApJ, 859, 33
Garrod, R. T., & Herbst, E. 2006, A&A, 457, 927
Geppert, W. D., Hamberg, M., Thomas, R. D., et al. 2006, Faraday Discuss., 133, 177
Griffin, M. J., Abergel, A., Abreu, A., et al. 2010, A&A, 518, L3
Harju, J., Pineda, J. E., Vasyunin, A. I., et al. 2020, ApJ, 895, 101
Herbst, E., & van Dishoeck, E. F. 2009, ARA&A, 47, 427
Hildebrand, R. H. 1983, QJRAS, 24, 267
Kamegai, K., Ikeda, M., Maezawa, H., et al. 2003, ApJ, 589, 378
Kawamura, A., Kun, M., Onishi, T., et al. 2001, PASJ, 53, 1097
Keto, E., & Caselli, P. 2008, ApJ, 683, 238
Keto, E., & Caselli, P. 2010, MNRAS, 402, 1625
Keto, E., Caselli, P., & Rawlings, J. 2015, MNRAS, 446, 3731
Kim, J., Cho, S.-H., & Kim, S. J. 2013, AJ, 145, 22
Kwok, S., Volk, K., & Bidelman, W. P. 1997, ApJS, 112, 557
Lee, J.-E., Bergin, E. A., & Evans, N. J., II 2004, ApJ, 617, 360
Mangum, J. G., & Shirley, Y. L. 2015, PASP, 127, 266
Müller, H. S. P., Schlöder, F., Stutzki, J., & Winnewisser, G. 2005, J. Mol. Struct., 742, 215
Nagy, Z., Spezzano, S., Caselli, P., et al. 2019, A&A, 630, A136
Ortiz-León, G. N., Loinard, L., Dzib, S. A., et al. 2018, ApJ, 869, L33
Pety, J. 2005, SF2A-2005: Semaine de l'Astrophysique Francaise, 721
Preibisch, T., & Mamajek, E. 2008, Handbook of Star Forming Regions (San francisco: ASP), Volume II, 235
Punanova, A., Caselli, P., Feng, S., et al. 2018, ApJ, 855, 112
Redaelli, E., Bizzocchi, L., Caselli, P., et al. 2018, A&A, 617, A7
Redaelli, E., Bizzocchi, L., Caselli, P., et al. 2019, A&A, 629, A15
Schöier, F. L., van der Tak, F. F. S., van Dishoeck, E. F., & Black, J. H. 2005, A&A, 432, 369
Soma, T., Sakai, N., Watanabe, Y., & Yamamoto, S. 2015, ApJ, 802, 74
Spezzano, S., Bizzocchi, L., Caselli, P., Harju, J., & Brünken, S. 2016, A&A, 592, L11
Spezzano, S., Caselli, P., Bizzocchi, L., Giuliano, B. M., & Lattanzi, V. 2017, A&A, 606, A82
Tafalla, M., & Santiago, J. 2004, A&A, 414, L53
Tafalla, M., Santiago-García, J., Myers, P. C., et al. 2006, A&A, 455, 577
van der Tak, F. F. S., Black, J. H., Schöier, F. L., et al. 2007, A&A, 468, 627
Vastel, C., Ceccarelli, C., Lefloch, B., & Bachiller, R. 2014, ApJ, 795, L2
Vastel, C., Bottinelli, S., Caux, E., et al. 2015, SF2A-2015: Proceedings of the Annual Meeting of the French Society of Astronomy and Astrophysics, 313
Vasyunin, A. I., Caselli, P., Dulieu, F., & Jiménez-Serra, I. 2017, ApJ, 842, 33
Watanabe, N., & Kouchi, A. 2002, ApJ, 571, L173

Appendix A: Additional emission maps

We present here additional maps observed with the IRAM 30 m telescope towards the six starless cores in our sample (see Fig. A.1). The properties of the observed transitions are listed in Table 5.

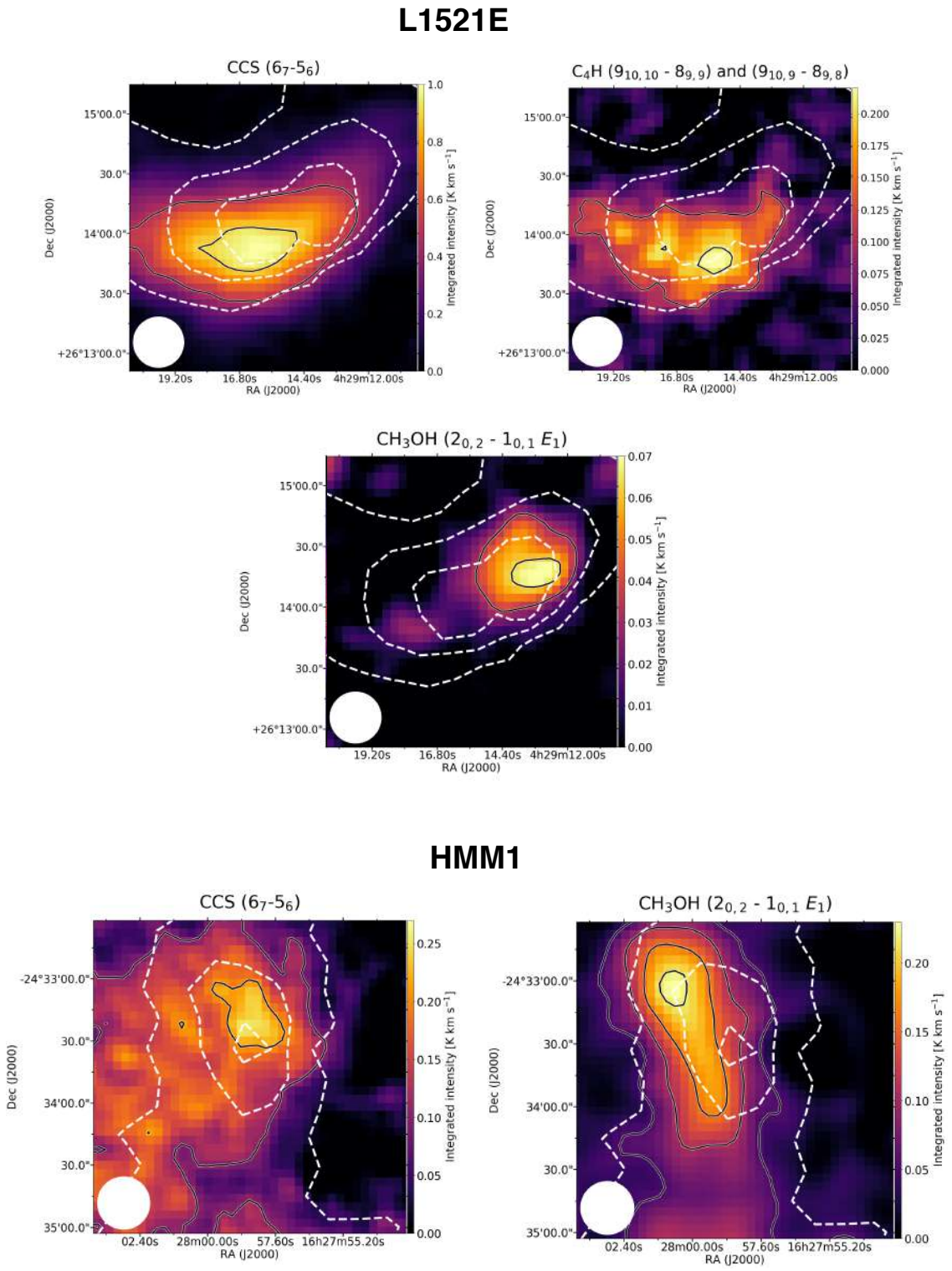

Fig. A.1. Integrated emission maps of CCS and C_4H towards the sources in our sample. The solid line contours indicate 90 and 50% of the integrated intensity peak with the exception of the C_4H transition in L429, where the contours indicate 90 and 70% of the integrated intensity peak. The dashed line contours represent the A_V values computed from the *Herschel*/SPIRE maps (5, 10, and 15 mag for B68; 20, 40, and 70 mag for L429; 10, 15, and 20 mag for L1521E; 20, 40, and 80 mag for L694-2; 20, 40, and 60 mag for HMM-1; 20, 30, and 40 mag for OphD). The white circle in the bottom left of each panel shows the 40″ beam of the SPIRE data.

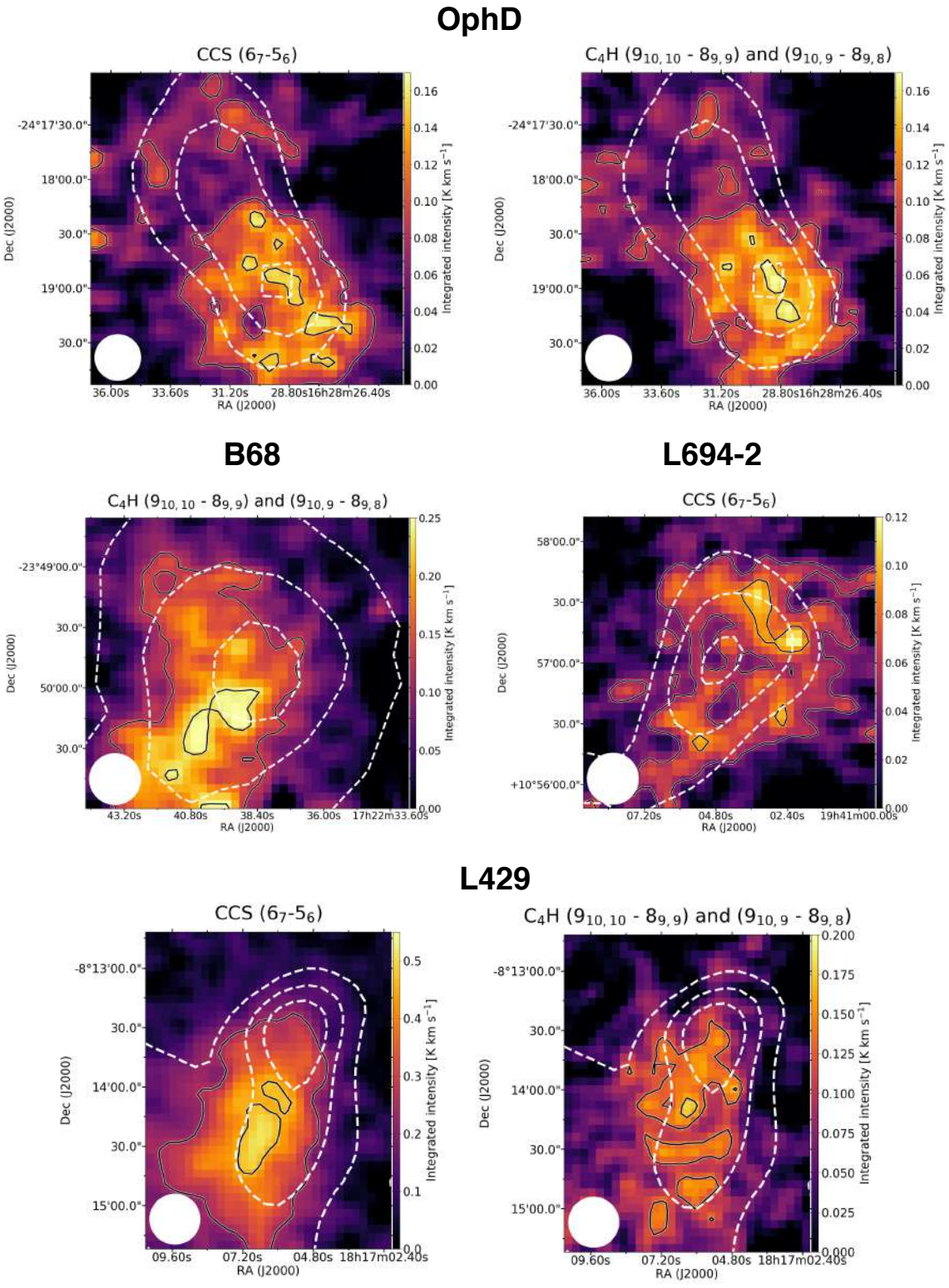

Fig. A.1. continued.

Appendix B: T_{dust} maps

The T_{dust} maps of the cores in our sample were computed together with the H_2 column density from *Herschel*/SPIRE data at 250, 350, and 500 μm (see Fig. B.1). For details see Sect. 2.3.

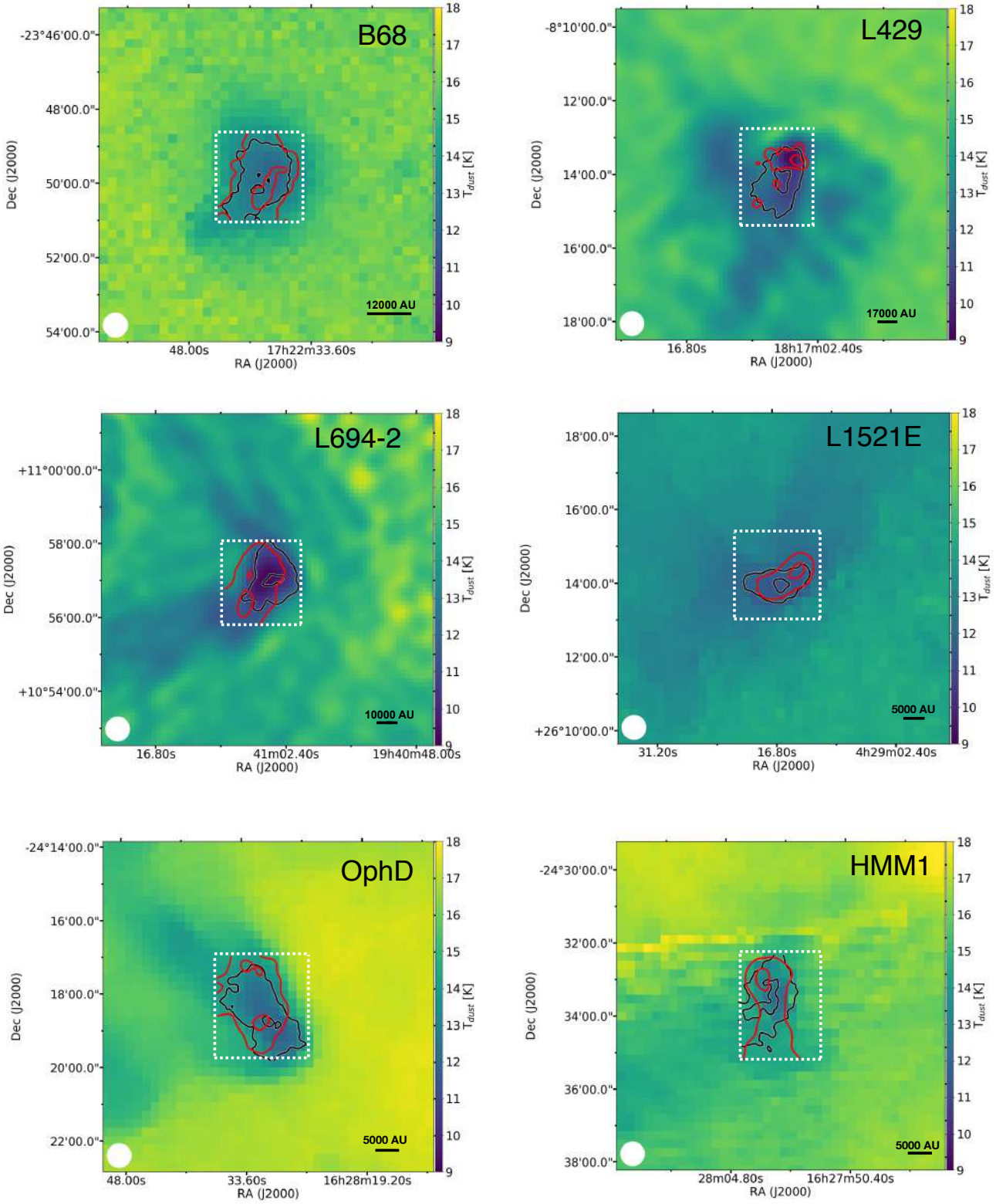

Fig. B.1. $T_{\rm dust}$ maps computed from *Herschel* SPIRE data. The red and black contours represent 90 and 50% of the integrated intensity peak of CH_3OH and c-C_3H_2, respectively. The dotted white box indicates the region mapped with the 30 m telescope.

Appendix C: Non-LTE effects on the $N(CH_3OH)/N(c\text{-}C_3H_2)$ abundance ratio

Assuming the typical core conditions ($T_k = 10$ K, $\Delta v = 0.5$ km s^{-1}), three $N(CH_3OH)/N(c\text{-}C_3H_2)$ abundance ratios that cover the range shown in Fig. 4, we ran RADEX for different densities between 1×10^4 and 1×10^6 cm^{-3}, covering the full range of densities in our sample. For each density and each abundance ratio, we looked at the RADEX prediction for the intensity of the $2_{1,2}$–$1_{1,1}$ (E_2) methanol line and the $2_{0,2}$–$1_{0,1}$ cyclopropenylidene line. Using CASSIS and the LTE approximation with $T_{\rm ex} = 10$ K, we then estimated the CH_3OH and

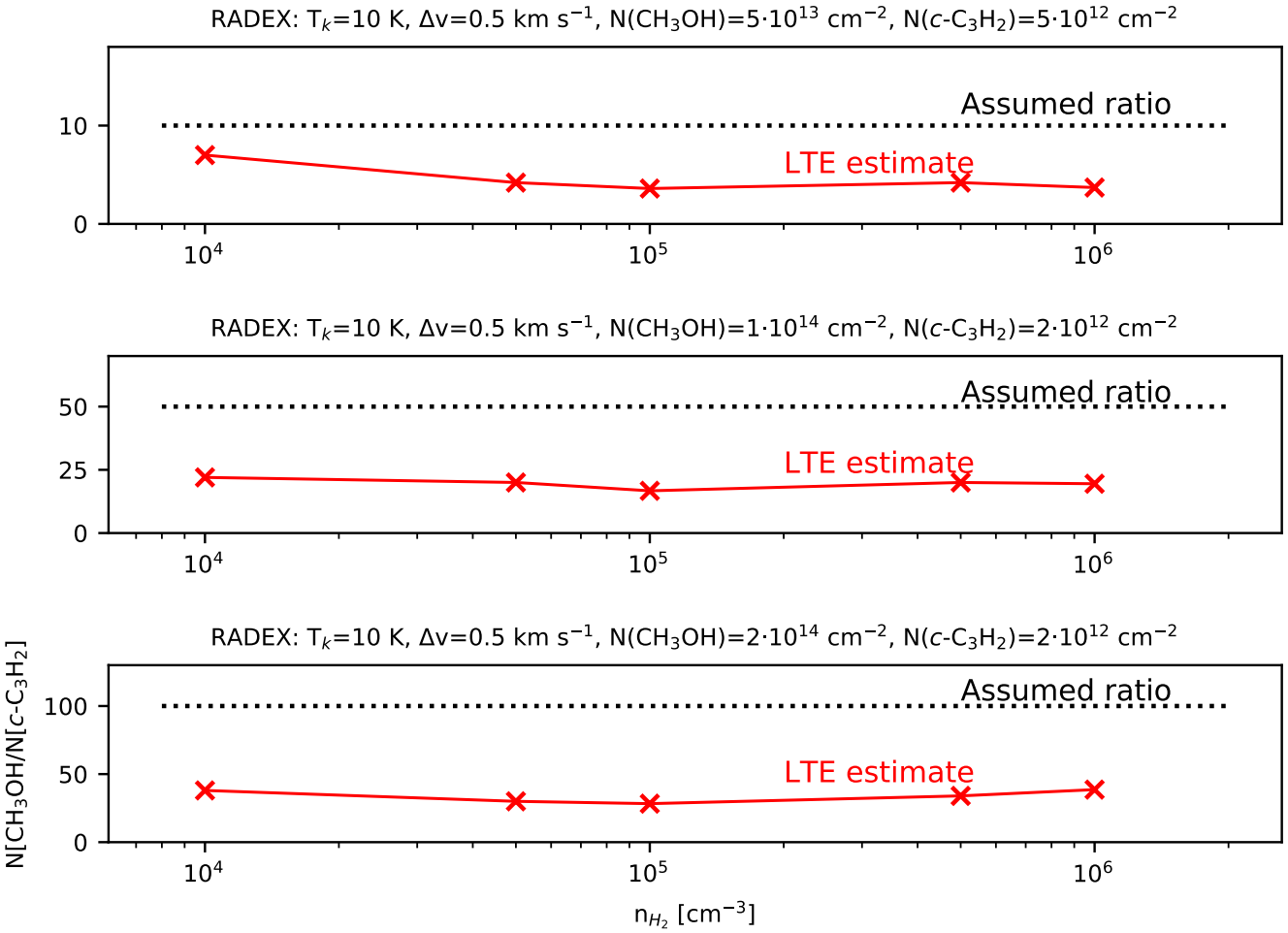

Fig. C.1. Variation of non-LTE effects on the $N(CH_3OH)/N(c\text{-}C_3H_2)$ abundance ratio at different volume densities. The intensities of the $2_{1,2}$–$1_{1,1}$ (E_2) methanol line and the $2_{0,2}$–$1_{0,1}$ cyclopropenylidene line were calculated using RADEX at different volume densities, and assuming different ratios (shown as a horizontal dashed line in each panel). The parameters used for the RADEX calculations are shown at the top of each panel. The red crosses show the abundance ratios resulting from the column densities that have been calculated to reproduce the intensities derived with RADEX, assuming LTE and $T_{ex} = 10$ K.

c-C_3H_2 column densities that reproduce the intensities derived from RADEX. Figure C.1 shows the intensity ratios calculated from the LTE approximation (red crosses) and the ratio assumed for the RADEX calculations (dashed horizontal lines). The LTE assumption underestimates the ratio by a factor of 2–3, but it does not show large variations within the volume densities covered. This means that the abundance ratio trends that we show in Fig. 4 are not going to be affected substantially by non-LTE effects.